AGU PUBLICATIONS

JGR

Journal of Geophysical Research: Space Physics

RESEARCH ARTICLE

10.1002/2014JA019837

Key Points:
- We present maps of thermospheric mass density dynamics during substorms
- The average thermospheric mass density increase in response to substorms is 4%
- We conclude that the average substorm deposits 30 GW in the polar thermosphere

Correspondence to:
L. B. N. Clausen,
lasse.clausen@fys.uio.no

Citation:
Clausen, L. B. N., S. E. Milan, and A. Grocott (2014), Thermospheric density perturbations in response to substorms, *J. Geophys. Res. Space Physics*, *119*, doi:10.1002/2014JA019837.

Received 30 JAN 2014
Accepted 10 MAY 2014
Accepted article online 16 MAY 2014

Thermospheric density perturbations in response to substorms

L. B. N. Clausen[1], S. E. Milan[2], and A. Grocott[3]

[1]Department of Physics, University of Oslo, Oslo, Norway, [2]Department of Physics and Astronomy, University of Leicester, Leicester, UK, [3]Department of Physics, Lancaster University, Lancaster, UK

Abstract We use 5 years (2001–2005) of CHAMP (Challenging Minisatellite Payload) satellite data to study average spatial and temporal mass density perturbations caused by magnetospheric substorms in the thermosphere. Using statistics from 2306 substorms to construct superposed epoch time series, we find that the largest average increase in mass density of about 6% occurs about 90 min after substorm expansion phase onset about 3 h of magnetic local time east of the onset region. Averaged over the entire polar auroral region, a mass density increase of about 4% is observed. Using a simple model to estimate the mass density increase at the satellite altitude, we find that an energy deposition rate of 30 GW applied for half an hour predominantly at an altitude of 110 km is able to produce mass density enhancements of the same magnitude. When taking into account previous work that has shown that 80% of the total energy input is due to Joule heating, i.e., enhanced electric fields, whereas 20% is due to precipitation of mainly electrons, our results suggest that the average substorm deposits about 6 GW in the polar thermosphere through particle precipitation. Our result is in good agreement with simultaneous measurements of the NOAA Polar-orbiting Operational Environmental Satellite (POES) Hemispheric Power Index; however, it is about 1 order of magnitude less than reported previously.

1. Introduction

Several attempts to characterize the response of the neutral atmosphere above 60 km altitude (the thermosphere) to magnetic substorms have been made in the past. It is intuitively clear that the energy carried by particles precipitating during substorms will, via a variety of mechanisms, eventually contribute to heating the neutral gas. Local heating will cause the neutral atmosphere to expand, and hence changes in the mass density at constant altitudes can be expected.

Prölss [1982] presented measurements from ESRO 4 which showed strong changes in composition in response to energy input from the magnetosphere into the polar thermosphere during magnetospheric substorms. Their results showed that, for a given altitude, the densities of the heavier neutral species like Ar and N_2 significantly increased about 4 h after the substorm onset. At the same time, the density of lighter species like He decreased, which led to an overall increase in mass density [*Prölss et al.*, 1988].

Data from the CHAMP satellite was used by *Ritter et al.* [2010] to estimate the impact of substorms on the mass density at about 400 km altitude. They compared mass density data along consecutive orbits (about 90 min apart) using the measurements just before substorm onset as the baseline to compare later orbits to. According to their results the mass density increased in the polar regions by about 4% to 15%, depending on the *Kp* index. Their results suggest that the mass density enhancement subsequently traveled to lower latitudes, forming a mass density bulge at the equator about 4 h after substorm onset.

Rees et al. [1983] modeled the impact of energetic (up to 10 keV) electron precipitation on the thermosphere and found that about half the energy carried by the electrons is passed on to the neutral gas. This energy transfer is not, as might be expected, accomplished directly by collisions but rather via a complicated path involving first ionization and dissociation and later excitation, ion/neutral chemistry, and collisional deactivations. *Richards* [2013] reports that the neutral heating efficiency is even lower (about 40%) and that the excess energy is either radiated or lost in the dissociation of O_2 because oxygen atoms do not recombine in the thermosphere.

It has become clear that the increase in thermospheric temperature and hence the increase in neutral density at constant altitude in response to magnetospheric forcing is caused by three mechanisms: (1) heating of the neutrals by precipitating particles as described above; (2) Joule heating due to enhanced electric

fields; and (3) momentum transfer via transient neutral-ion drag. Generally speaking, the response of the thermosphere to local energy deposition causes an initial local increase in temperature and subsequently neutral winds in all three directions (upward, zonal, and meridional). These increases in wind, temperature, and density propagate away from the heating region in the form of a wave [*Richmond and Matsushita*, 1975]. This wave is predicted to propagate over the poles between the hemispheres and interact differently with the background thermosphere and ionosphere depending on local time and other parameters [*Fuller-Rowell et al.*, 1994]. Indeed, such propagating density bulges have been reported by *Ritter et al.* [2010]. Using a 2-D model, *Chang and St.-Maurice* [1991] studied the dynamics of the winds and the temperature in response to enhanced electric fields, i.e., Joule heating. They found a neutral gas temperature increase in the region of strong electric fields, but above that region the temperature decreased. They attributed this effect to the strong vertical winds in that region that advected heat away from the heating region. Meridionally, the temperature increase was correlated to the propagation of the winds in that direction.

The thermospheric response is of course dependent on the nature and characteristics of the precipitating particles. These are conveniently combined into a single parameter, the total precipitation power U_A, which gives the total power input into the polar thermosphere. Several studies have tried to quantify this number, each yielding quite different results. *Ahn et al.* [1983] used ground-based magnetometers to infer what they called the "global particle energy injection rate" by using empirical relations between the magnetic north-south perturbation, the Hall conductivity, and U_A. They found that the energy injection rate is linearly related to the *AE* index. For a typical substorm with a maximum *AE* index of 300 nT, their work predicts a U_A of about 20 GW. Their estimates also showed that the Joule heat production rate due to strong electric fields is generally larger than the precipitation power by a factor of 4.

Combining measurements from two instruments on board the Polar spacecraft, *Østgaard et al.* [2002] estimated the hemispheric energy deposition rate by precipitating electrons during seven substorms. On average, they found values for U_A around 100 GW, i.e., the input by precipitating electrons was found to be about 2–4 times larger than that reported by earlier studies.

Using data from several auroral imagers on board the IMAGE satellite, *Hubert et al.* [2002] not only estimated U_A during several events of strong solar wind-magnetosphere coupling, but they were also able to distinguish between contributions from precipitating protons and electrons. They found that whenever the precipitation power peaked at values around 50 to 100 GW, the electron contribution to U_A was largest at about 80%.

Tanskanen et al. [2005] compared estimates of U_A derived from spacecraft auroral imaging data with hemispheric energy deposition rates derived from global MHD simulations and found that the temporal dynamics of the two matched reasonably well, whereas the absolute values were quite different. This in accordance with the results of *Østgaard et al.* [2002], who presented estimates derived from auroral data of about 150 GW, while MHD simulations predicted only 5 GW, i.e., a difference by a factor of 30. This large discrepancy between empirically derived values for U_A and estimates extracted from global MHD modeling was further discussed by *Palmroth et al.* [2004], who presented model results for a moderate substorm. According to *Palmroth et al.* [2004], the maximum precipitation power reached during this substorm was between 10 and 20 GW.

Another polar region where the thermospheric mass density is affected by particle precipitation, albeit not generated through substorms, is the cusp density enhancement first reported by *Lühr et al.* [2004]. Using data from the CHAMP satellite, they showed a significant (about 50%) mass density increase in the vicinity of the magnetospheric cusp. Later, using the 3-D global ionosphere-thermosphere model, *Deng et al.* [2013] showed that this density enhancement could be explained by a combination of Poynting flux due to small-scale wave activity and soft electron precipitation (about 200 eV).

In this paper we study the average temporal and spatial mass density perturbation at about 400 km altitude in response to magnetospheric substorms in order to estimate the energy input into the polar thermosphere during these events.

2. Methodology

The thermospheric mass density measurements presented here were obtained by the accelerometer on board the CHAMP (Challenging Minisatellite Payload) satellite. CHAMP was launched into a circular,

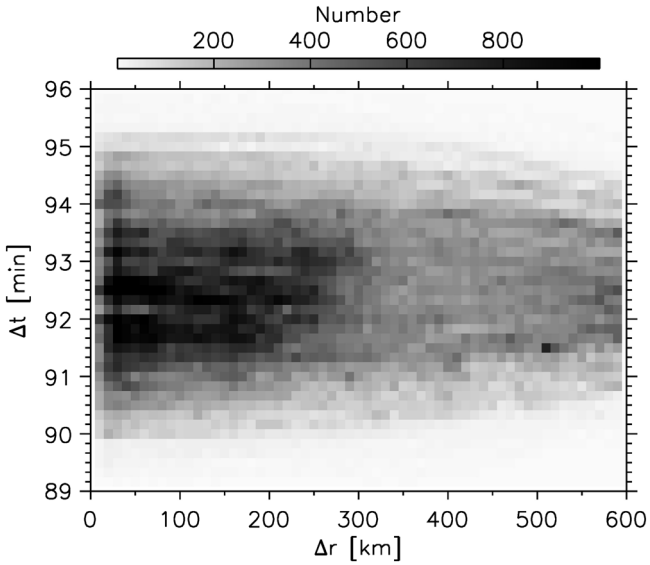

Figure 1. Two-dimensional histogram of the spatial and temporal distance between points on subsequent orbits, Δr and Δt, respectively. Most points used to find the relative mass density perturbation $\Delta\rho$ are located less than 300 km apart (in MLAT/MLT coordinates) and are separated by an average of 92.5 min.

near-polar (inclination: 87.2°) orbit at about 450 km altitude [*Reigber et al.*, 2002]. The orbital period of CHAMP was about 92 min, and its orbit precessed through local time at a rate of about 1 h per 11 days, or about 0.1° per orbit. The accelerometer was located at the satellite's center of gravity and measured the nongravitational forces by balancing a proof mass in the center of a vacuum cage by electrostatic forces. The thermospheric mass density ρ can be calculated from the acceleration experienced by the satellite in the direction of motion [*Doornbos et al.*, 2010]. The CHAMP data used here has a cadence of 10 s which, at an orbital speed of about 7.5 km/s, corresponds to a latitudinal resolution of about 75 km or 0.7°.

As a first step in our analysis, we transform the satellite positions into Altitude Adjusted Corrected Geomagnetic Coordinates latitude (MLAT)/magnetic local time (MLT) coordinates [*Baker and Wing*, 1989]. From each mass density measurement ρ we then calculate the density perturbation as the difference between the instantaneous ρ and the mass density measured at roughly the same location during the previous orbit, ρ_{po}. This calculation is sensible because of the relatively small precession rate of the spacecraft even in the MLAT/MLT coordinate frame and the good latitudinal resolution. In order to account for data gaps and varying dipole tilt, we only accept those cases where the distance Δr between the current location and the location during the previous orbit was less than 600 km in MLAT/MLT coordinates, which is roughly the latitudinal bin size of the spatial grid that we are using later (the grid size is 6° MLAT by 1200 km in longitude/MLT, which corresponds to roughly 2 h of MLT in the auroral zone). The relative mass density perturbation $\Delta\hat{\rho}$ is then calculated as

$$\Delta\hat{\rho} = 100\,\frac{\rho - \rho_{po}}{\rho_{po}}, \tag{1}$$

i.e., $\Delta\hat{\rho}$ represents the percentage change in mass density at a certain location with respect to the mass density measured at the same location during the previous orbit. Therefore, $\Delta\hat{\rho}$ has units of percent change per orbit. To convert this into more accessible units, we divide $\Delta\hat{\rho}$ by the time difference between ρ_{po} and ρ, i.e., the instantaneous orbital period Δt, to obtain $\Delta\rho'$ in units of percent change per minute:

$$\Delta\rho' = \frac{\Delta\hat{\rho}}{\Delta t}. \tag{2}$$

This step amounts to linearly interpolating the rate of change of the mass density at a certain location between the measurement made during the previous orbit and the current one.

Figure 1 shows a two-dimensional histogram of Δr and Δt. There are over 600,000 mass density measurements included in this study, and the figure shows that most points used for the determination of $\Delta\rho'$ are located less than 300 km apart (in MLAT/MLT coordinates) and are separated by an average of 92.5 min.

The reason behind using the rate of change of the relative mass density perturbation $\Delta\rho'$ instead of ρ in this study is to minimize influences of large-scale spatial variations of the neutral mass density and dynamics due to local time, satellite altitude changes, global magnetic activity levels, and changing solar radiation energy input as a result of the solar cycle. When comparing the effect of substorms, the background thermospheric mass density at substorm onset might be significantly different due to, e.g., differences in solar forcing; however, we expect the relative change to be comparable. With our methodology we hope to exclude the long-term variability in the background of the thermospheric mass density because all of these

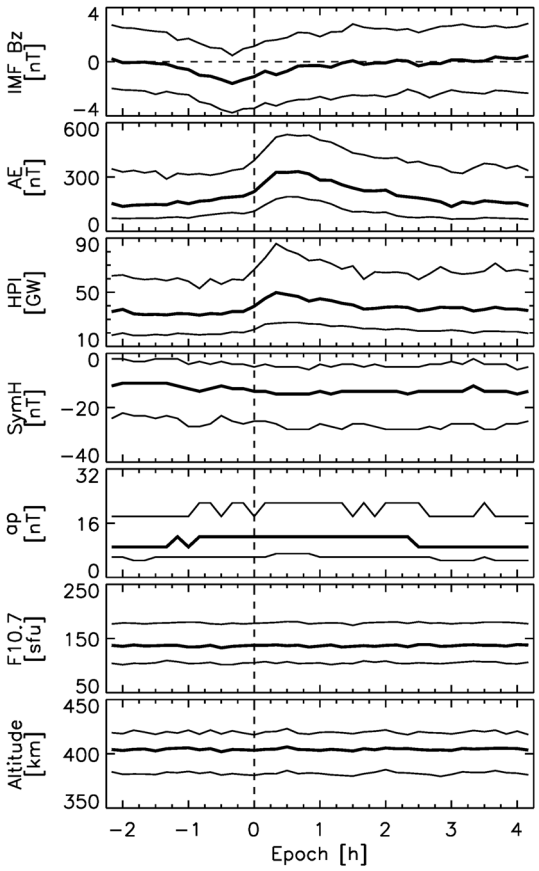

Figure 2. Overview of the median values (thick line) of (first to seventh panels) several magnetospheric activity parameters and CHAMP orbit characteristics as a function of epoch time relative to substorm expansion phase onset marked by a vertical dashed line based on 2306 onsets. The parameter's name is given in the *y* axis label. Thinner lines give the upper and lower quartiles of the distribution in each epoch bin.

influences are small on the time scales of one orbital period (about 92 min). Note that our determination of $\Delta\rho'$ is similar to the method of *Ritter et al.* [2010]; however, we calculate a density perturbation for every single point based on the measurement made at that position during the previous orbit; *Ritter et al.* [2010] normalized all subsequent orbits by the density values observed along the last orbit prior to substorm onset. We also stress that we do not scale the mass density measurements to a common altitude, which is often done when using CHAMP mass density data.

All CHAMP mass density perturbation measurements are then binned on a spatial grid in MLAT/MLT coordinates. The spatial grid we employ consists of roughly equal-area bins which, at the magnetic equator, are 6° MLAT × 10° MLT.

As a last step, we then construct superposed epoch time series for each spatial bin b by finding the median value $\langle\Delta\rho'(b,t)\rangle$ of the rate of change of the relative mass density perturbation $\Delta\rho'(b,t)$ at each time step t relative to substorm expansion phase onset. We start our time series 2 h before onset and followed the mass density variation all the way to 4 h after the start of the substorm. We have experimented with longer time spans, up to 8 h following substorm expansion phase onset, but found that the mass density variations did not change significantly beyond 4 h after onset, suggesting that the thermosphere had returned to equilibrium at that point. Once constructed, the superposed epoch time series of the median rate of change of the mass density perturbation $\langle\Delta\rho'(b,t)\rangle$ can easily be integrated in order to find the mass density perturbation $\Delta\rho(b,t)$ in a superposed epoch sense relative to some arbitrary starting point t_s in a certain spacial bin b:

$$\Delta\rho(b,t) = \sum_{i=0}^{k} \left\langle \Delta\rho'(b, t_s + i\delta t) \right\rangle \cdot \delta t, \tag{3}$$

where $t = t_s + k\delta t$ and δt is the time resolution of our analysis, which is 10 min. The starting point we use is the average mass density perturbation 135 min before substorm expansion phase onset.

The goal of this study is to investigate the temporal and spatial evolution of thermospheric mass density perturbations $\Delta\rho$ during different phases of substorms. *Frey et al.* [2004] identified 2437 substorms occurring between May 2000 and December 2002 using the FUV instrument [*Mende et al.*, 2000a, 2000b] on the IMAGE spacecraft, subsequently extending this number to 4193 after considering the 5 year period up to the end of the IMAGE mission in December 2005. For the purpose of this study we refine this list to 2306 isolated substorms between January 2001 and December 2005 by excluding those events which had another substorm occurring within 4 h after expansion phase onset. Furthermore, we assume that substorms are, on average, conjugate phenomena; i.e., if the IMAGE spacecraft observed a substorm at −67.3° MLAT in the Southern Hemisphere, we assume that at the same time a substorm occurred in the Northern Hemisphere at +67.3° MLAT. According to a study by *Østgaard et al.* [2011] the interhemispheric MLT offset of substorms depends

on the interplanetary magnetic field (IMF) By component. However, according to this study, the offset is smaller than 1 h MLT even for large By-dominated cases (Bz $\approx$ 0 nT and By $\geq$ 10 nT). Since the zonal extent of our spatial grid around the onset latitudes is larger than 1 h MLT, it is unlikely that the results shown here are influenced by our assumption of conjugacy. For all substorms in our refined list we then perform a superposed epoch analysis of the CHAMP-derived mass density perturbations in the Northern Hemisphere as described above.

3. Observations

Figure 2 shows an overview of several magnetospheric activity parameters and CHAMP orbital characteristics as a function of substorm onset epoch time including all 2306 isolated substorm onsets from the Frey list. From top to bottom, we show the IMF Bz component as an indicator for solar wind-magnetosphere coupling on the dayside, the *AE* index as a measure of substorm strength, the *SYM-H* index as a measure for the ring current intensity, the NOAA POES Hemispheric Power Index (HPI) estimating the power deposited in the polar regions by energetic particles, the global magnetospheric magnetic activity index *ap*, the $F_{10.7}$ parameter as an indicator for solar energy input, and finally the altitude of the CHAMP spacecraft. In each panel thick lines give the median value during each time step of the superposed epoch analysis and thinner lines give the upper and lower quartiles. A vertical dashed line marks the epoch time of substorm expansion phase onset as extracted from the auroral observations made by IMAGE.

Prior to substorm expansion phase onset the median of the IMF Bz component (Figure 2, first panel) decreases to a minimum value of about −2 nT, which indicates energy input into the magnetosphere via dayside reconnection. A significant increase in the substorm indicator *AE* (Figure 2, second panel) points toward an increase in auroral electrojet activity just after onset, consistent with the increase in auroral activity observed by the IMAGE spacecraft used to time individual substorm onsets. The NOAA POES Hemispheric Power Index (HPI), shown in Figure 2 (third panel), is calculated from spectra of energetic particles between 50 eV and 20 keV measured on board the NOAA POES satellites during transits over the poles; its median values indicate that the average substorm deposits an extra 10 GW in the polar regions; here again the estimates from the Southern Hemisphere are mapped into the Northern Hemisphere. There is a slight strengthening of the ring current during the substorm growth phase as indicated by a small decrease of about 2 nT of the *SYM-H* index, again indicative of energy input from the solar wind into the magnetospheric system. The *SYM-H* value remains essentially constant during the expansion and recovery phase. We also observe a slight variation of the median *ap* value around substorm onset, increasing from 8 to 12 nT 1 h before onset and decreasing back to 8 nT about 2 h into the recovery phase. Note, however, that the $F_{10.7}$ parameter and the satellite altitude are on average constant over the substorm intervals, indicating that mass density measurements made by CHAMP during substorms are not systematically influenced by variability in the solar radiation input into the thermosphere or by satellite altitude. This is true despite the 5 years investigated in this study (2001–2005) covering the maximum and declining phases of solar cycle 23 and despite the satellite altitude decreasing from 450 km to 355 km during this time.

As outlined in section 2, for each time step of our epoch analysis we collect all $\Delta\rho'$ within a spatial grid in the Northern Hemisphere, find their median value, and integrate the time series to obtain the relative mass density perturbation $\Delta\rho$ within each bin above 40° MLAT. The result is shown in Figure 3. The epoch time is given on top of each panel, concentric rings mark the magnetic latitude starting at 80° MLAT in 20° steps, radial black lines mark each third hour of MLT, and the Sun (12 MLT) is to the top of each panel. Bins below 60° MLAT contain about 100 measurements, around 60° MLAT each bin contains about 500 measurements, whereas there are over 1000 points in each bin above 80° MLAT. The median value of the mass density perturbations between −6% and 6% in each bin is color-coded according to the color bar above the figure with negative perturbations colored blue and positive perturbations colored red. A black cross in the premidnight sector around 65° MLAT marks the average onset location as determined from the IMAGE observations.

As can be seen in Figure 3 up until 30 min before substorm onset the relative density perturbation fluctuates around 0% across the northern polar region, indicating no change in thermospheric mass density at about 400 km altitude during this time. On the dayside, between 12 and 16 MLT and centered at about 70° MLAT, we observe an increase in relative mass density starting about 30 min before substorm expansion phase onset. On the nightside, the mass density is steady up until substorm expansion phase onset, after which

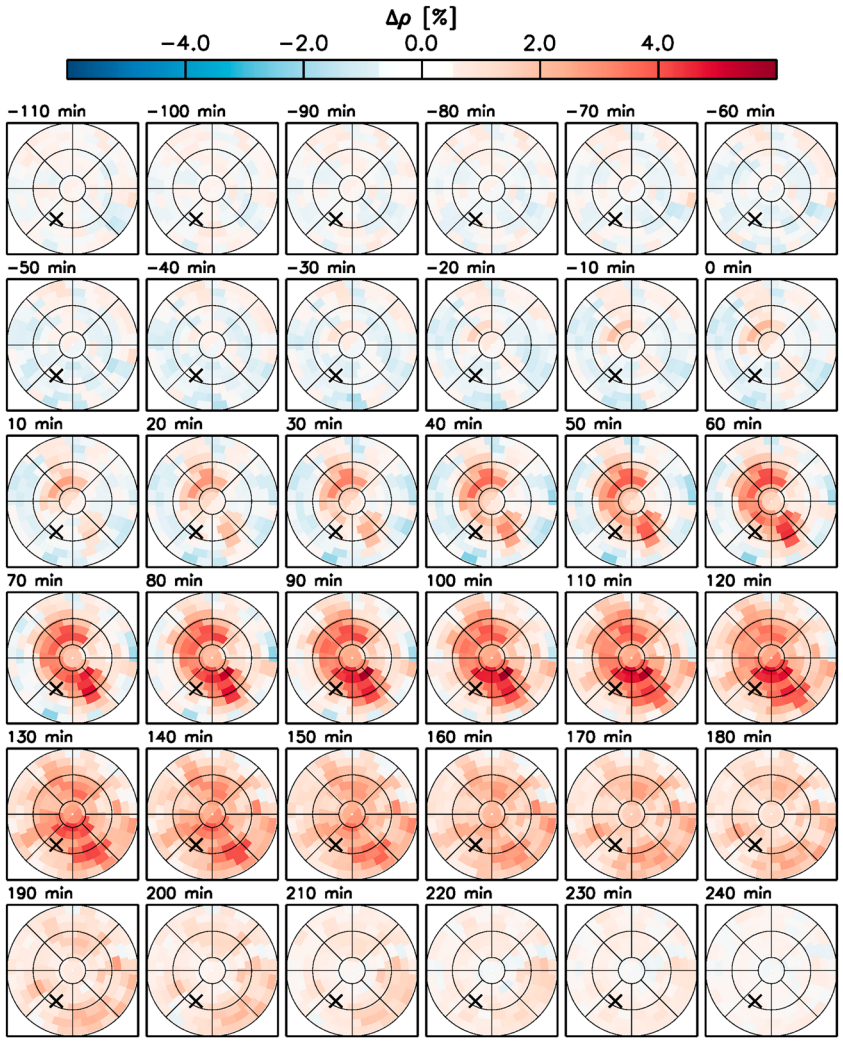

Figure 3. Spatial variation of the relative mass density perturbation $\Delta\rho$ in the Northern Hemisphere at certain substorm epoch times on a magnetic latitude/magnetic local time grid; mass density increases are colored red, mass density decreases are colored blue. The Sun (12 MLT) is to the top, dawn is to the right, and dusk is to the left. Concentric rings give the magnetic latitude in 20° steps starting at 80° MLAT; radial black lines mark each third hour of MLT. The epoch time is given on top of each panel. The black cross marks the median location of all 2306 substorm expansion phase onsets.

it quickly (within 20 min after onset) increases. Note that the region in which the largest increase occurs is located about 10° poleward and about 3 h of MLT eastward of the average substorm onset location. It peaks around 01 MLT and 70° MLAT about 90 min after substorm onset. In the subsequent time steps, the relative mass density enhancement weakens but spreads over the entire polar region; 4 h after substorm onset, the mass density perturbation returns to values around 0%.

In order to estimate the mass density perturbations in the auroral zone on a larger scale, we show the average values of $\Delta\rho$ in four local time sectors between 65° and 75° MLAT and over the entire polar auroral region between 65° and 75° MLAT as a function of epoch time in Figure 4. The values shown in Figure 4 are obtained by finding the average value of $\Delta\rho'$ in these five spatial bins and integrating the resulting time series, as described earlier. From top to bottom, this figure shows $\Delta\rho$ between 09 and 15 MLT (Figure 4a, dayside), between 15 and 21 MLT (Figure 4b, dusk), between 21 and 03 MLT (Figure 4c, nightside), and between 03 and 09 MLT (Figure 4d, dawn). Figure 4e shows $\Delta\rho$ across the northern polar auroral region. For all five local time sectors we only include values between 65° and 75° MLAT in order to focus on changes in the auroral zone. Substorm expansion phase onset is marked by a vertical dashed line, and zero perturbation is marked by a horizontal dashed line. Thick lines show the mean of the distribution in each epoch bin, and

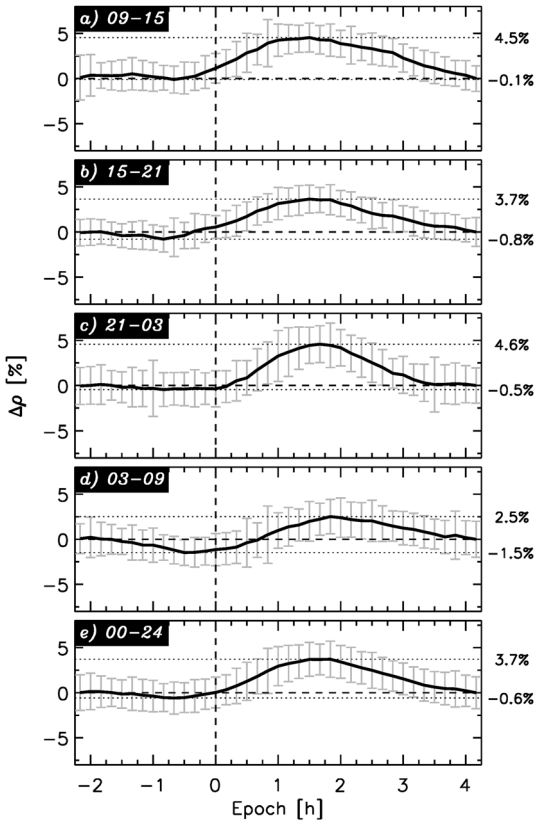

Figure 4. The relative density perturbation $\Delta\rho$ in the Northern Hemisphere between 65° and 75° MLAT in four local time sectors averaged over 2306 substorm onsets: (a) between 09 and 15 MLT (dayside), (b) between 15 and 21 MLT (dusk), (c) between 21 and 03 MLT (nightside), and (d) between 03 and 09 MLT (dawn) as a function of epoch time. (e) $\Delta\rho$ across the entire polar auroral region between 65° and 75° MLAT. Substorm expansion phase onset is marked by a vertical dashed line, zero perturbation is marked by a horizontal dashed line. The standard deviations of the distributions in each epoch bin are indicated by gray bars. Thin dotted lines mark the maximum and minimum of $\Delta\rho$, and these values are given to the right of each panel.

the gray bars indicate the standard deviation in each bin. The thin dotted lines mark the maximum and minimum of the mass density perturbation which is given to the right of each panel.

As previously documented in Figure 3, on the dayside the mass density begins to increase around 30 min before substorm onset to about 2% at onset, and it peaks 1 h after onset at a value of 4.5%; between 1 and 2 h after onset the perturbation is relatively constant at that level and then decreases back to 0%, indicating a return to presubstorm mass density values in this local time sector. In the dusk sector, there is a similar preonset increase, albeit slightly later, and the post-onset maximum at about 3.5% is reached also about 1 h after onset. The plateau and recovery to preonset mass density values is also observed. The nightside increase begins (from slightly negative values) at onset and peaks about 90 min after onset at a maximum mass density perturbation of 4.6%. In the ensuing 90 min, the mass density perturbation recovers to preonset values. The dawn sector shows the smallest positive mass density perturbation; however, there is a significant negative perturbation starting about 90 min before onset and continuing to about 45 min after onset. The maximum perturbation at below 3% is reached 2 h after onset and subsequently recovers to preonset values. Finally, the overall mass density perturbation between 65° and 75° MLAT shows a composite of all local time sectors discussed earlier: a slight increase before onset, the maximum at about 2 h after onset, and the recovery to preonset values of the mass density between 2 and 4 h after onset.

In contrast to the finer scale results of Figure 3, Figure 4 allows us to easily estimate the total mass density increase during a substorm across the polar auroral region which is, at its maximum, just below 4% when averaged over all MLTs and almost 5% localized around magnetic midnight and on the dayside.

As documented above, substorms have a significant effect on the thermospheric mass density around 400 km altitude. During the 5 years covered by this study the CHAMP altitude decreased from about 450 km to about 355 km. This gives us the unique opportunity to study the altitude dependence of $\Delta\rho$; because substorms are a nightside phenomenon, we focus on the nightside auroral region between 65° and 75° MLAT and between 21 and 03 MLT (compare Figure 4d). In Figure 5 we show averages of the CHAMP altitude, several magnetospheric activity parameters, and the mass density as well as its perturbation in the nightside auroral sector as a function of epoch time grouped by satellite altitude. Averages of measurements within each altitude bin are plotted using the same color, and the standard deviations of all values within each epoch bin are indicated by gray bars. The satellite altitude decreases (Figure 5, first row) from left to right, and so does the average solar flux level (Figure 5, second row). This is due to the fact that grouping CHAMP measurements by altitude essentially corresponds to sorting by time, because the satellite continuously lost altitude due to drag, such that higher altitude measurements were made around the year 2001, i.e., during solar maximum, whereas lower altitude measurements were made mainly during 2005, when

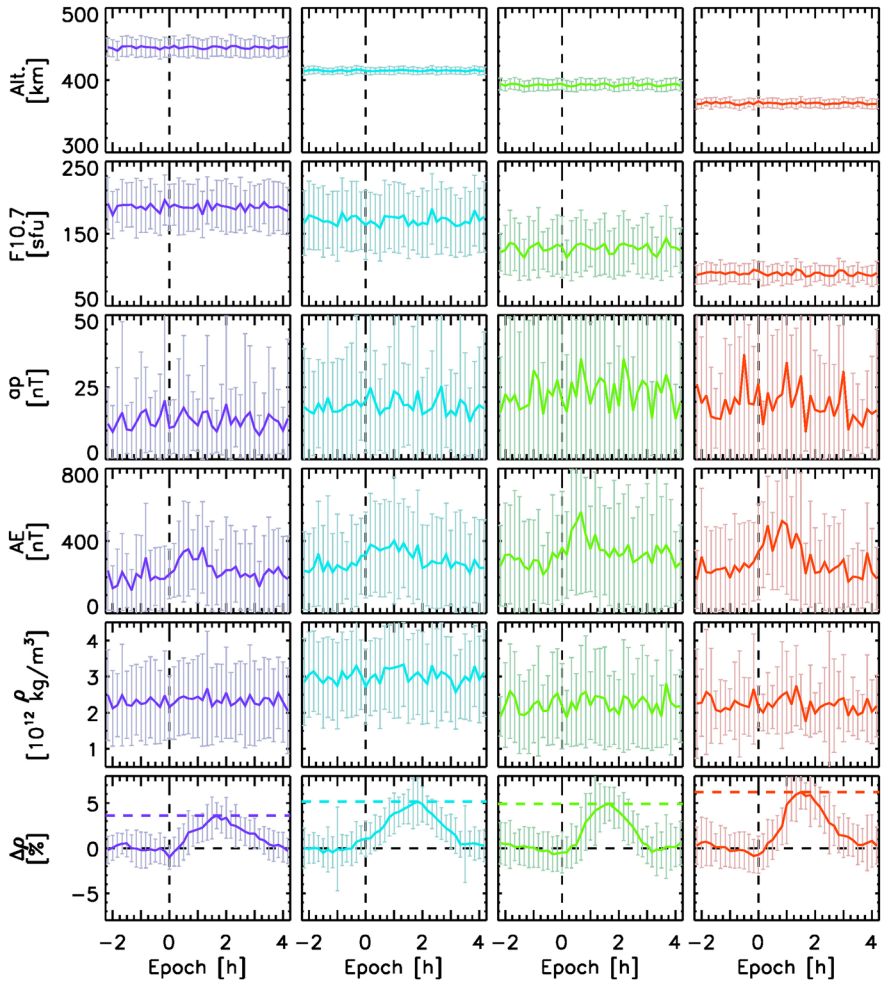

Figure 5. (first to sixth rows) Averages of CHAMP altitude and geomagnetic activity indicators, as well as the mass density and its perturbation in the nightside auroral region between 65° and 75° MLAT and between 21 and 03 MLT grouped by CHAMP altitude. The parameter is given in the *y* axis of each row, and the gray bars indicate the standard deviation in each epoch bin.

the solar cycle was approaching solar minimum. This dynamic is also evident in the average geomagnetic indices, *ap* and *AE*, which are highest in the middle to lowest altitude ranges, i.e., during the declining phase of solar cycle 23. Due to a combination of the decreasing altitude of the satellite and the decrease in solar EUV flux, the absolute mass density measured by CHAMP stays essentially constant (Figure 5, fifth row). The mass density perturbation in the nightside auroral zone shown in Figure 5 (sixth row) indicates that the perturbation amplitude increases with decreasing altitude and is highest at the lowest altitudes around 360 km. However, it should be noted that the average substorm (see fourth row of panels in Figure 5) is also largest in that altitude bin, and that the difference in $\Delta\rho$ between the highest and lowest density bin is within their respective standard deviations. Furthermore, only the measurements made in the nightside auroral sector indicate a coherent altitude dependence; producing a figure like Figure 5 for the measurements made in the other three MLT sectors or averaging over all local times in the auroral zone shows no altitude dependence of the $\Delta\rho$ response.

4. Discussion

We have investigated the perturbation of the thermospheric mass density in response to substorms. We find that substorms do have, as expected, an influence on the thermospheric density distribution. The mass density locally increased by up to 6% in a region located about 3 h of MLT east of the average substorm expansion phase onset location, i.e., the location of initial auroral brightening. The increase in mass density

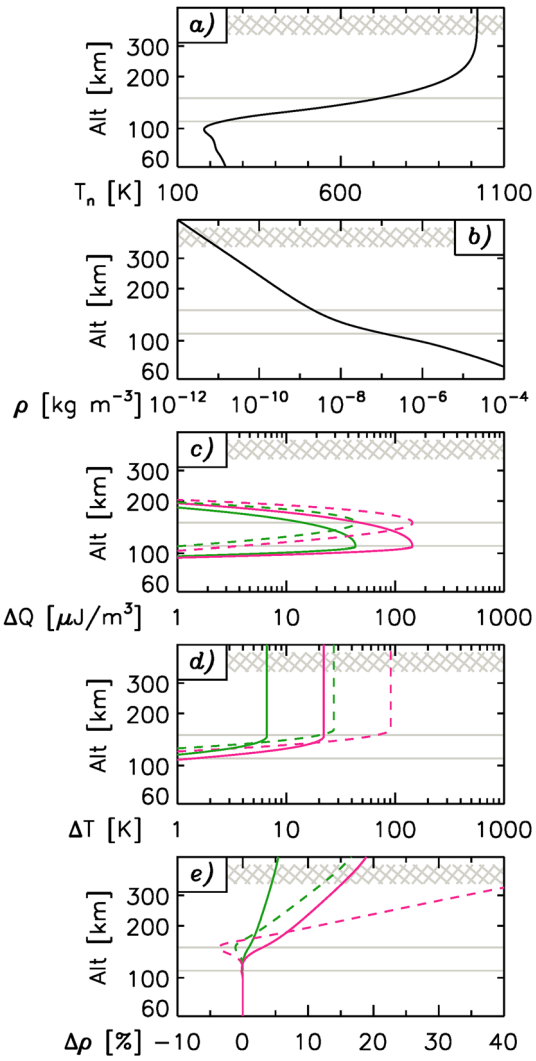

Figure 6. The altitude dependence of (a, b) the neutral temperature and mass density, (c) the modeled energy input, (d) the expected neutral temperature increase, and (e) the resulting mass density perturbation. The hashed gray region marks the altitude range of the CHAMP satellite between 2001 and 2005. The horizontal gray lines give the two altitudes of maximum energy input into the thermosphere at 110 and 150 km, and the solid and dashed lines give the modeled parameters, respectively. The green lines assume a total power input of 30 GW, whereas the red lines give the results when 100 GW is deposited in the thermosphere. See text for more details.

appears on a time scale of less than 20 min after expansion phase onset. It reaches its maximum about 90 min after the substorm onset. When averaged over the entire polar auroral region between 65° and 75° MLAT, we find that the thermospheric mass density increase is smaller than local increases, only about 4%.

Ritter et al. [2010] used a similar technique of comparing mass density changes during subsequent orbits in relation to substorm onsets selected from the "Frey onset list." However, they produced averages of single orbital passes and not the 2-D spatial coverage that we show in Figure 6; also, they compared data along subsequent orbits and hence achieved a time resolution of one orbital period, i.e., around 90 min. They found a mass density increase in the vicinity of the substorm onset region of about 15% for 67 substorms during $Kp > 4$ and about 4% for 110 substorms during $Kp \leq 2$. Their results are in good agreement with ours which are averages over all *Kp* conditions.

Our superposed epoch study shows a significant thermospheric mass density increase prior to substorm onset in the dayside and dusk sectors (see Figures 3 and 4). The spot that brightens, i.e., the location where the mass density increase is strongest, is situated postnoon at a latitude of about 72° MLAT. The increase begins about 30 min, maybe even 40 min, before substorm onset, roughly at the same time the IMF Bz component (Figure 2, first panel) dips significantly toward more negative values. This dip indicates increased dayside reconnection and, more importantly, more particle precipitation in the cusp region [*Frey et al.*, 2003]. Increased cusp precipitation has previously been linked to neutral upwelling in the cusp region [*Lühr et al.*, 2004; *Deng et al.*, 2013]. The shift toward the dusk sector can be explained by the influence of the IMF By component on the location of cusp precipitation [*Newell et al.*, 1989; *Lockwood et al.*, 2003]; during the substorms used in this study, the median IMF By component was positive throughout (not shown).

On the nightside, the largest increase in mass density is observed about 90 min after onset; interestingly, the location of the largest perturbation is not located at the substorm onset location as determined from global auroral imaging but some 3 h of MLT east of that location in the postmidnight sector. *Hardy et al.* [1985] showed maps of the energy flux associated with precipitating particles at energies between 50 eV and 20 keV, derived from the low-orbiting DMSP satellites. These polar maps showed a clear maximum of energy flux into the auroral zone in the postmidnight sector, colocated with the maximum mass density perturbation we observe. *Hardy et al.* [1985] binned their results by *Kp* and showed that the intensity of the maximum changed with *Kp*; however, its location did not. Similar results for the energy flux of precipitating auroral

particles were obtained by *Newell et al.* [2010], who binned by substorm epoch time. *Newell et al.* [2010] showed that after substorm onset the energy flux of monoenergetic particle precipitation (also called "inverted V" precipitation) peaked in the premidnight sector, colocated with the substorm onset location, i.e., location of maximum brightness of auroral emissions. However, the maximum of the energy flux was found to be located postmidnight, caused by diffuse auroral precipitation, again in the vicinity of maximum $\Delta\rho$ shown in Figure 3. Furthermore, *Newell et al.* [2010] showed that the total energy flux of the diffuse aurora amounted to about 4 times the power input associated with monoenergetic precipitation; it follows that the largest mass density increase due to particle precipitation is expected to be located in the postmidnight sector.

Precipitating particles are just one of the sources which heat the thermosphere during magnetospheric substorms; the others are Joule heating and neutral-ion drag. Joule heating occurs when enhanced electric fields drive ions through the neutral atmosphere; its heating effect decreases as the neutrals slowly pick up the ion velocity. Once the enhancement of the external electric field fades away during the recovery phase of substorms, the ion velocity decreases, whereas the neutrals continue to convect due to their higher inertia. This leads to heating via neutral-ion drag, as now the neutrals are streaming through the slower ion gas; this is sometimes referred to as the "flywheel effect" [*Banks*, 1972].

The energy deposition rate due to Joule heating is proportional $n_e n_n(\vec{v} - \vec{u})^2$, where n_e is the plasma density, n_n is the neutral density, and $\vec{v}$ and $\vec{u}$ are the ion and neutral velocities, respectively [*Schunk and Nagy*, 2000]. Using a global ionosphere-thermosphere model, *Deng and Ridley* [2007] found the largest Joule heating energy deposition rates due to large differences in the direction of neutral and ion velocity in the postmidnight sector, again in the direct vicinity of the largest mass density increase observed in our study.

In an attempt to model the effects on the upper neutral atmosphere during substorms, *Richmond and Matsushita* [1975] used a two-dimensional ionosphere-thermosphere model. They predicted temperature increases of the neutral gas of over 100 K and observed large wave-like disturbances in neutral winds that propagated from the heating region in the auroral zone across the pole and toward the equator. These wind disturbances show both features described above: the delayed response of the neutral motion to the enhanced electric field as well as the flywheel effect, which both contributed to thermospheric heating. It should be noted that the substorm they simulated was very powerful with electric fields of 100 mV/m and a total energy flux into the auroral zone of almost 1000 GW. *Fuller-Rowell et al.* [1994] simulated the thermospheric response to storms, using a global coupled ionosphere-thermosphere model. They confirmed the results of *Richmond and Matsushita* [1975], highlighting the complexity of the thermospheric response due to the different time scales involved in the heating. They also emphasized the importance of vertical winds which in their study contributed to the distribution of heated neutrals in both the zonal and meridional directions.

In light of the previous work presented above, it is prudent to assume that the substorm-induced thermospheric mass density enhancements observed in this study were most likely due to heating of the neutral atmosphere by particle precipitation and Joule heating. In the next paragraphs we will estimate the mass density increase caused by input of different amounts of energy deposited at various altitudes with the help of a simple model.

If the neutral atmosphere is in diffusive equilibrium, then the particle density n as a function of altitude h above some reference altitude h_0 is given by

$$n(h) = n(h_0)\frac{T(h_0)}{T(h)}\exp\left\{-\int_{h_0}^{h}\frac{\bar{m}(z)g(z)}{k_B T(z)}\mathrm{d}z\right\}, \tag{4}$$

where T is the neutral temperature, $\bar{m}$ is the average neutral particle mass, g is the gravitational acceleration, and k_B is Boltzmann's constant. Supplying the neutral particles at some altitude h with a certain amount of thermal energy ΔQ (in J/m^3) will locally change the temperature by

$$\Delta T(h) = \Delta Q(h)/c_p(h), \tag{5}$$

where $c_p(h)$ is the heat capacity at constant pressure of the neutral gas in units of J/K/m^3. Assuming each neutral particle has a heat capacity of $k_B(f/2+1)$, where f is the number of degrees of freedom, then $c_p(h)$ is simply the particle's heat capacity multiplied by the neutral particle number density n:

$$c_p(h) = n(h)k_B\left(\frac{f}{2}+1\right). \tag{6}$$

Assuming for the sake of simplicity that an average substorm distributes a total amount of energy E equally over the entire auroral oval of area A_o, we can estimate the input energy per area. Although substorms are a nightside phenomenon, this assumption is not too outrageous as significant amounts of energy are deposited on the dayside due to enhanced ion convection and also particle precipitation [*Deng and Ridley*, 2007; *Newell et al.*, 2010]. The local input energy per unit volume $\Delta Q(h)$ can then be estimated after including an estimate of how the total energy per unit area E/A_o is deposited at different altitudes. In the following, we will focus on the effect of precipitating electrons; note, however, that similar arguments can be made for Joule heating such that our results are applicable to any mechanism that deposits a certain amount of energy per unit volume in the thermosphere. Furthermore, the energy deposition rate due to Joule heating is proportional to $n_e n_n(\vec{v}-\vec{u})^2$ and hence peaks at the altitude of the $n_e{}^* n_n$ peak [*Schunk and Nagy*, 2000]. During substorms the electron density in the E region is greatly enhanced and often larger than the F region peak [*Bates and Hunsucker*, 1974], such that the E region is also where most of the energy associated with Joule heating is deposited [*Deng and Ridley*, 2007].

Precipitating electrons with certain energies deposit most of their energy at a certain altitude, e.g., 10 keV electrons deposit most of their energy at about 110 km [e. g., *Luhmann*, 1995], and therefore $\Delta Q(h)$ depends on the spectrum of the precipitating electrons. Instead of modeling the spectrum, we introduce the unitless parameter f_{ed} which describes how big a fraction of the incoming energy per unit area is deposited at a certain altitude. We assume that f_{ed} has a maximum at some altitude h_m. In our model f_{ed} decreases by about 5 orders of magnitude, i.e., f_{ed} essentially decreases to zero, toward lower altitudes, reaching this limit at an altitude of 85 km. This part of f_{ed} accounts for higher energy precipitation up to about 100 keV which penetrates deeper into the neutral atmosphere. For the lower part of the energy spectrum of the precipitating particles, we assume that f_{ed} decreases by 5 orders of magnitude between h_m and 220 km, which corresponds to the penetration depth of electrons with energies around 10 eV. On both sides of h_m the functional dependence of f_{ed} is assumed to be that of a Gaussian. Using these above assumptions [e. g., *Rees et al.*, 1983; *Sotirelis and Newell*, 2000], we can estimate the energy density ΔQ as a function of altitude h as

$$\Delta Q(h) = \frac{f_{ed}(h)}{F}\frac{E}{A_o \Delta h}, \tag{7}$$

where $F = \int f_{ed}(h)\mathrm{d}h$ is a normalization factor for f_{ed} and Δh is the altitude range over which $\Delta Q(h)$ is applied. Again, the shape, location, and extent of f_{ed} were made for electron precipitation; however, similar arguments, i.e., there exists an altitude at which the energy deposition is maximum, hold for altitude-dependent Joule heating.

Rees et al. [1983] found, using a much more sophisticated 1-D model than ours, that electron precipitation had a neutral heating efficiency of about 50%, i.e., about half of the precipitation energy was converted into neutral heating. Furthermore, *Rees et al.* [1983] found that this result was, below about 220 km, nearly independent of the spectrum of the electron precipitation. Using time-dependent modeling, they also showed that, under constant energy input due to precipitation, the thermosphere reached a quasi-equilibrium heating efficiency after about 3 min. We incorporate these results in our model by dividing $\Delta Q(h)$ by 2.

Using (7), (6), and (5), we can calculate the altitude profile of the temperature increase for a given energy input E. According to our assumptions, the temperature increase will be zero above 220 km because ΔQ is zero there. However, previous studies have shown that vertical heat conduction is very effective in altitude ranges above 100 km [*Roble and Dickinson*, 1973; *Forbes and Garrett*, 1979; *Chang and St.-Maurice*, 1991]. We account for the effective vertical heat transfer by setting ΔT to its maximum value at all altitudes above the peak in temperature increase.

Once we calculate the temperature increase as a function of altitude, we can evaluate the right-hand side of (4) to find the altered density profile $n_S(h)$, where the subscript S indicates that the profile accounts for the heating during substorms. Relating $n_S(h)$ to the original $n(h)$ then allows us to estimate the altitude profile of the relative particle density perturbation due to the deposition of a certain amount of energy E predominantly at an altitude h_m. Note that the relative particle density perturbation is the same as the relative mass density perturbation because we assume that the particle composition and hence $\bar{m}(h)$ are not affected by substorms. Figure 6 shows the result of these calculations, for two different energies E deposited at two different altitudes h_m. The main results of these model calculations are summarized in Table 1; the line colors/styles relate to the colors/styles used in Figure 6.

Table 1. Main Results of Model Calculations

U_A (GW)	h_m (km)	u_A (mW/m^2)	Max ΔT (K)	Max $\Delta\rho$ (%)	Color	Style
30	110	1.9	6.6	5.4	green	solid
30	150	1.9	22.1	18.9	green	dashed
100	110	6.4	27.3	16.6	red	solid
100	150	6.4	91.1	61.6	red	dashed

Figures 6a and 6b show the neutral temperature and mass density altitude profiles provided by the Naval Research Laboratory Mass Spectrometer and Incoherent Scatter Radar Extended (NRLMSISE) model [*Picone et al.*, 2002] for auroral latitudes on the nightside between 60 and 500 km altitude. The vertical resolution Δh is 1 km. These values are taken as the unperturbed background for our model calculations, i.e., $n(h)$; the NRLMSISE-00 model also provides the neutral particle composition needed to estimate $\bar{m}$ in (4). The average neutral particle composition from the NRLMSISE-00 model is also used to calculate f in (6) as the weighted average of the number of degrees of freedom for atomic and molecular species, which is 3 and 5, respectively.

In Figure 6c the energy deposition density $\Delta Q(h)$ is shown; the two green lines give the results of the model calculations for a total energy of 54 TJ (30 GW of power applied for half an hour) deposited over the entire auroral oval. The area of the annulus between 65° MLAT and 75° MLAT centered on the magnetic pole is used as an estimate for the size of the auroral oval A_o. Furthermore, the main energy deposition is assumed to occur at two different altitudes, 110 km (solid line) and 150 km (dashed line). These altitudes correspond to the penetration depths of electrons with energies of about 10 keV and 1 keV, respectively. The red lines (dashed and solid) show $\Delta Q(h)$ when we assume a total energy of 180 TJ (100 GW for half an hour) being deposited at those two altitudes. For references, 100 GW and 30 GW evenly distributed over the entire area between 65° MLAT to 75° MLAT corresponds to an input power density u_A of 6.4 mW/m^2 and 1.9 mW/m^2, respectively (see third column in Table 1). Figure 6d shows the resulting temperature increases in the four cases considered, taking into account the values from Figure 6c and the altitude-dependent heat capacity, which scales with the particle density (see fourth column in Table 1). As mentioned before, the good vertical thermal conductivity of the thermosphere is accounted for by setting ΔT to its maximum value above the peak altitude. In Figure 6e we show the resulting mass density perturbation (see fifth column in Table 1). In all panels the two deposition altitudes h_m are marked by horizontal gray lines, and the hashed region indicates the CHAMP altitude range between 350 and 450 km.

It is clear from our assumption of perfect vertical heat conduction that the density perturbation increases without bound as one moves up in altitude (see Figure 6e). This is indeed the opposite of the trend suggested by Figure 5 which indicates decreasing density perturbations at higher altitudes. *Deng and Ridley* [2007] used a coupled global ionosphere-thermosphere model to show that the energy deposition rate due to Joule heating peaked around 120 km altitude, i.e., at the altitude of maximum plasma density; however, the maximum heating rate (in K/s) was achieved at 350 km altitude, and this heating rate decreased toward lower and higher altitudes. The density perturbation scales with the heating rate, such that the observed decrease in $\Delta\rho$—if indeed it is statistically significant—could be explained by the peaked heating rate occurring below the CHAMP measurements.

Figure 6 shows that the altitude at which most energy is deposited has a strong impact on the resulting mass density perturbation at CHAMP altitude. The green solid and dashed lines, which represent 30 GW applied for half an hour deposited at 110 and 150 km altitude, respectively, show that the temperature increase in the case of the low-altitude deposition stays below 10 K (solid green line), whereas if the same amount of energy is deposited 40 km higher up, the temperature increases by more than 30 K (dashed green line). The same observation is true for the larger energy deposited shown by red solid and dashed lines. This is of course the result of the exponential decrease in mass density at those altitudes; as can be seen from Figure 6b, the density decreases by about 2 orders of magnitude between 110 and 150 km, such that if the same amount of energy is deposited at higher altitudes, fewer particles share the total energy such that the temperature increase per particle is much larger.

Of course, our model rests on many simplifying assumptions. It assumes only very basic heat transport from the heating site and neglects heat transport through either convection or horizontal conduction, and the neutral gas is assumed to remain in diffusive equilibrium. All of the mechanisms named above would act to decrease the portion of the total energy input transferred to the neutrals locally and hence weaken the mass

density increase above the heating region. However, comparing our theoretical estimates of temperature and density perturbations with results from much more sophisticated models, we see relatively good agreement. *Walterscheid et al.* [1985] simulated the thermospheric response of a stable auroral arc and observed temperature increases of 6 K at 210 km altitude in response to precipitating particles with an energy density ΔQ of up to 10 μJ/m^3 around 180 km altitude. Modeling the effect of soft electron precipitation (100 eV) at a rate of 2 mW/m^2, *Deng et al.* [2013] find a 25% density increase in neutral density at 400 km altitude. Such low-energy particles, however, deposit their energy at much larger altitudes (~200 km) such that a much larger effect on the density can be expected due to much lower neutral densities at those altitudes. When applying these inputs to our model, we predict a mass density enhancement at 400 km altitude of about 35%. In light of these severe limitations of our model it should be clear that the aim here is not to present an accurate description of the dynamical response of the thermosphere to magnetospheric energy deposition but to obtain a ballpark estimate of the energy input that can explain the observed mass density enhancement.

The calculations described above use the NRLMSISE-00 model to obtain an estimate for the altitude-dependent average neutral particle mass $\bar{m}$ to use in (4). Although this value is a function of altitude in our model, it is assumed to be constant with respect to substorm phase (or epoch time). This assumption might not be valid, as previous studies have shown that the composition in the polar (and indeed equatorial) thermosphere can be significantly altered during magnetically disturbed times [*Prölss*, 1982, 2011]. It is believed that local heating drives enhanced verticals winds, which do not perturb the diffusive equilibrium of the major constituent; however, they will affect minor species due to the difference in scale height. The effect is an increase in $\bar{m}$ above the heating region, which leads to a decrease of the overall scale height and hence a decrease in mass density. Most of the studies published to investigate this effect focus on periods of geomagnetic storms, i.e., intervals of large variations in the planetary index *ap*. As can be seen in Figure 2, during the substorm studied here, the *ap* index is relatively stable throughout the substorm intervals (an *ap* index of 12 nT corresponds to a *Kp* index of 3-). The time scales of composition changes induced by geomagnetic activity are of the order of 1 h or more [*Prölss*, 2011]. In our time series of the mass density perturbation within the northern polar region (see Figure 4), however, we observe no permanent decline of the thermospheric mass density at CHAMP altitudes, even hours after the substorm onset.

Figure 4 shows that according to CHAMP measurements the mass density increase over the northern auroral oval between 65° and 75° MLAT in response to substorms is 4%. According to our model results, depositing 100 GW over half an hour in the auroral region at any altitude would cause generally bigger mass density increases. On the other hand, if a total of 30 GW is predominantly deposited at 110 km altitude for the same amount of time, the expected mass density increase would match our observations. Previous studies have suggested [*Deng and Ridley*, 2007] that the altitude profile of the energy deposition rate due to particle precipitation and due to Joule heating are quite similar; however, *Ahn et al.* [1983] estimated the magnitude of the deposition rate due to Joule heating to be about a factor of 4 larger than U_A. The fact that the location of maximum mass density increase is displaced from the substorm onset position also suggests a larger influence of electric fields at that location and is consistent with previous studies. *Grocott et al.* [2009] have shown that the ionospheric convection does indeed increase in response to substorms, albeit with a 30–45 min delay for larger substorms. We conclude from our model that a combined energy flux of 30 GW due to both particle precipitation and Joule heating applied over half an hour can produce the observed mass density perturbation in the thermosphere.

Previous work has provided quite different estimates for the power input U_A of particle precipitation during substorms, which of course multiplied by the average substorm length gives the total precipitation energy input into the polar region, i.e., the *E* in (7). Whereas *Palmroth et al.* [2004] reported precipitation powers of about 10 to 20 GW, both *Østgaard et al.* [2002] and *Tanskanen et al.* [2002] estimated U_A around 100 GW. *Newell et al.* [2010] showed that the increase in energy flux carried by three different types of aurora increased on average by a combined 10 GW. The results of *Palmroth et al.* [2004] and *Newell et al.* [2010] are consistent with our superposed epoch analysis of the HPI shown in Figure 2 (third panel) which suggests an increase in hemispheric power of about 10 GW in response to substorms. Assuming that, as *Østgaard et al.* [2002] and others suggested, a typical substorm deposits about 100 GW in the polar thermosphere just through electron precipitation and adding 400 GW due to Joule heating caused by enhanced electric fields, there seems to be a stark contrast of the expected and the observed mass density enhancement at 400 km altitude.

Our simple model shows that, if 30 GW (6 GW for precipitating particles and 24 GW for Joule heating) were applied for 30 min at 110 km altitude and half the energy was expended heating the neutrals, the theoretical and observed mass density perturbations match well around 6%. This of course raises the interesting question why the values for U_A derived from our study, auroral images, and MHD modeling are significantly different. Future studies might help understand this discrepancy.

5. Summary

We investigate the temporal and spatial variation of average thermospheric mass density perturbations at an altitude around 400 km in response to magnetospheric substorms based on 2306 expansion phase onsets. We find that substorms have a significant effect on the thermosphere by increasing the mass density by about 4% over the entire polar region about 90 min after onset. Locally, the mass density increases by up to 6%. Interestingly, the location of maximum mass density increase is not colocated with the region of brightest aurora but lies about 3 h of MLT east of the average substorm onset location. This is indicative of the importance of diffuse auroral precipitation (as opposed to inverted V type precipitation) which also peaks in the postmidnight sector and also suggests enhanced Joule heating in that sector. Using a simple 1-D model, we find that a total power density of about 2 mW/m^2 applied predominantly at an altitude of 110 km can account for mass density increases of that magnitude. By total we mean the combined input from particle precipitation and Joule heating. If such an energy deposition rate were to be realized over the entire auroral oval, then the average substorm would deposit about 30 GW. As the ratio of energy input from precipitation to Joule heating is thought to be about 1 to 4, our results suggest that particle precipitation during average substorms amounts to about 6 GW of power input. We also find that the altitude at which the energy is deposited plays a crucial role in the thermospheric response. Summarizing our results, it seems more likely that through particle precipitation the average substorm deposits around 10 GW of power over half an hour than 100 GW over the same time span as suggested by some studies.

Acknowledgments

The CHAMP data used in this study can be downloaded free of charge from http://thermosphere.tudelft.nl/acceldrag/. All geomagnetic indices are available at http://cdaweb.gsfc.nasa.gov/. The hemispheric power index (HPI) is available at http://www.swpc.noaa.gov/ftpmenu/lists/hpi.html. The authors would like to acknowledge S. E. Haaland and J. K. Burchill for fruitful discussions during the 2013 CaNoRock STEP PhD school.

Alan Rodger thanks the reviewers for their assistance in evaluating this paper.

References

Ahn, B.-H., S.-I. Akasofu, and Y. Kamide (1983), The Joule heat production rate and the particle energy injection rate as a function of the geomagnetic indices *AE* and *AL*, *J. Geophys. Res.*, *88*, 6275–6287, doi:10.1029/JA088iA08p06275.

Baker, K. B., and S. Wing (1989), A new magnetic coordinate system for conjugate studies at high latitudes, *J. Geophys. Res.*, *94*, 9139–9143, doi:10.1029/JA094iA07p09139.

Banks, P. M. (1972), Magnetospheric processes and the behavior of the neutral atmosphere, in *Space Research Conference*, edited by S. A. Bowhill, L. D. Jaffe, and M. J. Rycroft, pp. 1051–1067, Akademie-Verlag GmbH, Berlin, Germany.

Bates, H. F., and R. D. Hunsucker (1974), Quiet and disturbed electron density profiles in the auroral zone ionosphere, *Radio Sci.*, *9*, 455–467, doi:10.1029/RS009i004p00455.

Chang, C. A., and J.-P. St.-Maurice (1991), Two-dimensional high-latitude thermospheric modeling—A comparison between moderate and extremely disturbed conditions, *Can. J. Phys.*, *69*, 1007–1031, doi:10.1139/p91-159.

Deng, Y., and A. J. Ridley (2007), Possible reasons for underestimating Joule heating in global models: *E* field variability, spatial resolution, and vertical velocity, *J. Geophys. Res.*, *112*, A09308, doi:10.1029/2006JA012006.

Deng, Y., T. J. Fuller-Rowell, A. J. Ridley, D. Knipp, and R. E. Lopez (2013), Theoretical study: Influence of different energy sources on the cusp neutral density enhancement, *J. Geophys. Res. Space Physics*, *118*, 2340–2349, doi:10.1002/jgra.50197.

Doornbos, E., et al. (2010), Neutral density and crosswind determination from arbitrarily oriented multiaxis accelerometers on satellites, *J. Spacecraft Rockets*, *47*, 580–589, doi:10.2514/1.48114.

Forbes, J. M., and H. B. Garrett (1979), Theoretical studies of atmospheric tides, *Rev. Geophys. Space Phys.*, *17*, 1951–1981, doi:10.1029/RG017i008p01951.

Frey, H. U., S. B. Mende, S. A. Fuselier, T. J. Immel, and N. Østgaard (2003), Proton aurora in the cusp during southward IMF, *J. Geophys. Res.*, *108*(A7), 1277, doi:10.1029/2003JA009861.

Frey, H. U., S. B. Mende, V. Angelopoulos, and E. F. Donovan (2004), Substorm onset observations by IMAGE-FUV, *J. Geophys. Res.*, *109*, A10304, doi:10.1029/2004JA010607.

Fuller-Rowell, T. J., M. V. Codrescu, R. J. Moffett, and S. Quegan (1994), Response of the thermosphere and ionosphere to geomagnetic storms, *J. Geophys. Res.*, *99*, 3893–3914, doi:10.1029/93JA02015.

Grocott, A., J. A. Wild, S. E. Milan, and T. K. Yeoman (2009), Superposed epoch analysis of the ionospheric convection evolution during substorms: Onset latitude dependence, *Ann. Geophys.*, *27*, 591–600, doi:10.5194/angeo-27-591-2009.

Hardy, D. A., M. S. Gussenhoven, and E. Holeman (1985), A statistical model of auroral electron precipitation, *J. Geophys. Res.*, *90*, 4229–4248, doi:10.1029/JA090iA05p04229.

Hubert, B., J.-C. Gérard, D. S. Evans, M. Meurant, S. B. Mende, H. U. Frey, and T. J. Immel (2002), Total electron and proton energy input during auroral substorms: Remote sensing with IMAGE-FUV, *J. Geophys. Res.*, *107*(A8), 1183, doi:10.1029/2001JA009229.

Lockwood, M., B. S. Lanchester, H. U. Frey, K. Throp, S. K. Morley, S. E. Milan, and M. Lester (2003), IMF control of cusp proton emission intensity and dayside convection: Implications for component and anti-parallel reconnection, *Ann. Geophys.*, *21*, 955–982, doi:10.5194/angeo-21-955-2003.

Luhmann, J. G. (1995), *Introduction to Space Physics,* chap. 7, pp. 183–202, Cambridge Univ. Press, Cambridge, U. K.

Lühr, H., M. Rother, W. Köhler, P. Ritter, and L. Grunwaldt (2004), Thermospheric up-welling in the cusp region: Evidence from CHAMP observations, *Geophys. Res. Lett.*, *31*, L06805, doi:10.1029/2003GL019314.

Mende, S. B., et al. (2000a), Far ultraviolet imaging from the IMAGE spacecraft. 1. System design, *Space Sci. Rev.*, *91*, 243–270.

Mende, S. B., et al. (2000b), Far ultraviolet imaging from the IMAGE spacecraft. 2. Wideband FUV imaging, *Space Sci. Rev.*, *91*, 271–285.
Newell, P. T., C.-I. Meng, D. G. Sibeck, and R. Lepping (1989), Some low-altitude cusp dependencies on the interplanetary magnetic field, *J. Geophys. Res.*, *94*, 8921–8927, doi:10.1029/JA094iA07p08921.
Newell, P. T., A. R. Lee, K. Liou, S.-I. Ohtani, T. Sotirelis, and S. Wing (2010), Substorm cycle dependence of various types of aurora, *J. Geophys. Res.*, *115*, A09226, doi:10.1029/2010JA015331.
Østgaard, N., G. Germany, J. Stadsnes, and R. R. Vondrak (2002), Energy analysis of substorms based on remote sensing techniques, solar wind measurements, and geomagnetic indices, *J. Geophys. Res.*, *107*(A9), 1233, doi:10.1029/2001JA002002.
Østgaard, N., K. M. Laundal, L. Juusola, A. Åsnes, S. E. Håland, and J. M. Weygand (2011), Interhemispherical asymmetry of substorm onset locations and the interplanetary magnetic field, *Geophys. Res. Lett.*, *38*, L08104, doi:10.1029/2011GL046767.
Palmroth, M., P. Janhunen, T. Pulkkinen, and H. Koskinen (2004), Ionospheric energy input as a function of solar wind parameters: Global MHD simulation results, *Ann. Geophys.*, *22*, 549–566, doi:10.5194/angeo-22-549-2004.
Picone, J. M., A. E. Hedin, D. P. Drob, and A. C. Aikin (2002), NRLMSISE-00 empirical model of the atmosphere: Statistical comparisons and scientific issues, *J. Geophys. Res.*, *107*(A12), 1468, doi:10.1029/2002JA009430.
Prölss, G. W. (1982), Perturbation of the low-latitude upper atmosphere during magnetic substorm activity, *J. Geophys. Res.*, *87*, 5260–5266, doi:10.1029/JA087iA07p05260.
Prölss, G. W. (2011), Density perturbations in the upper atmosphere caused by the dissipation of solar wind energy, *Surv. Geophys.*, *32*, 101–195, doi:10.1007/s10712-010-9104-0.
Prölss, G. W., M. Roemer, and J. W. Slowey (1988), Dissipation of solar wind energy in the earth's upper atmosphere—The geomagnetic activity effect, *Adv. Space Res.*, *8*, 215–261, doi:10.1016/0273-1177(88)90043-9.
Rees, M. H., K. Stamnes, B. A. Emery, and R. G. Roble (1983), Neutral and ion gas heating by auroral electron precipitation, *J. Geophys. Res.*, *88*, 6289–6300, doi:10.1029/JA088iA08p06289.
Reigber, C., H. Lühr, and P. Schwintzer (2002), CHAMP mission status, *Adv. Space Res.*, *30*, 129–134, doi:10.1016/S0273-1177(02)00276-4.
Richards, P. G. (2013), Reevaluation of thermosphere heating by auroral electrons, *Adv. Space Res.*, *51*, 610–619, doi:10.1016/j.asr.2011.09.004.
Richmond, A. D., and S. Matsushita (1975), Thermospheric response to a magnetic substorm, *J. Geophys. Res.*, *80*, 2839–2850, doi:10.1029/JA080i019p02839.
Ritter, P., H. Lühr, and E. Doornbos (2010), Substorm-related thermospheric density and wind disturbances derived from CHAMP observations, *Ann. Geophys.*, *28*, 1207–1220, doi:10.5194/angeo-28-1207-2010.
Roble, R. G., and R. E. Dickinson (1973), Is there enough solar extreme ultraviolet radiation to maintain the global mean thermospheric temperature? *J. Geophys. Res.*, *78*, 249–257, doi:10.1029/JA078i001p00249.
Schunk, R. W., and A. F. Nagy (2000), *Ionospheres: Physics, Plasma Physics, and Chemistry*, Cambridge Atmospheric and Space Science Series, Cambridge Univ. Press, Cambridge, U. K.
Sotirelis, T., and P. T. Newell (2000), Boundary-oriented electron precipitation model, *J. Geophys. Res.*, *105*, 18,655–18,673, doi:10.1029/1999JA000269.
Tanskanen, E., T. I. Pulkkinen, H. E. J. Koskinen, and J. A. Slavin (2002), Substorm energy budget during low and high solar activity: 1997 and 1999 compared, *J. Geophys. Res.*, *107*(A6), 1086, doi:10.1029/2001JA900153.
Tanskanen, E. I., M. Palmroth, T. I. Pulkkinen, H. E. J. Koskinen, P. Janhunen, N. Østgaard, J. A. Slavin, and K. Liou (2005), Energetics of a substorm on 15 August, 2001: Comparing empirical methods and a global MHD simulation, *Adv. Space Res.*, *36*, 1825–1829, doi:10.1016/j.asr.2004.05.013.
Walterscheid, R. L., L. R. Lyons, and K. E. Taylor (1985), The perturbed neutral circulation in the vicinity of a symmetric stable auroral arc, *J. Geophys. Res.*, *90*, 12,235–12,248, doi:10.1029/JA090iA12p12235.